Received: 3 October 2021 | Revised: 26 December 2021 | Accepted: 6 January 2022

DOI: 10.1002/elps.202100324

ELECTROPHORESIS

RESEARCH ARTICLE

AC electrokinetic immobilization of influenza virus

Sandra Stanke[1,2] | **Christian Wenger**[3,4] | **Frank F. Bier**[2] | **Ralph Hölzel**[1]

[1]Fraunhofer Institute for Cell Therapy and Immunology, Branch Bioanalytics and Bioprocesses (IZI-BB), Potsdam-Golm, Germany (Email: sandra.stanke@izi-bb.fraunhofer.de)

[2]Institute of Biochemistry and Biology, University of Potsdam, Potsdam-Golm, Germany

[3]IHP – Leibnizinstitut für innovative Mikroelektronik, Frankfurt/Oder, Germany

[4]Brandenburg University of Technology Cottbus–Senftenberg, Cottbus, Germany

Correspondence
Dr. Ralph Hölzel, Fraunhofer Institute for Cell Therapy and Immunology, Branch Bioanalytics and Bioprocesses (IZI-BB), 14476 Potsdam-Golm, Germany.
Email: ralph.hoelzel@izi-bb.fraunhofer.de

Funding information
Deutsche Forschungsgemeinschaft, Grant/Award Numbers: SPP1857, HO1298/4-1; European Regional Development Fund; Ministerium für Wissenschaft, Forschung und Kultur, Grant/Award Number: 85004117; German Academic Scholarship Foundation

Abstract

The use of alternating current (AC) electrokinetic forces, like dielectrophoresis and AC electroosmosis, as a simple and fast method to immobilize submicrometer objects onto nanoelectrode arrays is presented. Due to its medical relevance, the influenza virus is chosen as a model organism. One of the outstanding features is that the immobilization of viral material to the electrodes can be achieved permanently, allowing subsequent handling independently from the electrical setup. Thus, by using merely electric fields, we demonstrate that the need of prior chemical surface modification could become obsolete. The accumulation of viral material over time is observed by fluorescence microscopy. The influences of side effects like electrothermal fluid flow, causing a fluid motion above the electrodes and causing an intensity gradient within the electrode array, are discussed. Due to the improved resolution by combining fluorescence microscopy with deconvolution, it is shown that the viral material is mainly drawn to the electrode edge and to a lesser extent to the electrode surface. Finally, areas of application for this functionalization technique are presented.

KEYWORDS
AC electrokinetics, AC electroosmosis, dielectrophoresis, influenza virus, nanoelectrodes

1 | INTRODUCTION

A key aspect in biosensor design is the functionalization of the sensor surface with a bio-receptor. The purpose is to create an interface between the specific analyte and the transducer. A common method to functionalize the surface of biosensors is to use reagents with complementary functional groups at each end: one group that covalently binds to the biosensor surface and the other one forming a covalent bond with the bio-receptor. As an example, thiols and dithiols are used to functionalize gold surfaces. Thiol groups bind to the metal surface, whereas their tail- and terminal-functional groups protrude into the volume forming a self-assembled monolayer (SAM) [1]. The quality of the SAM formation depends, among others, on the cleanliness of the surface and multiple preparation steps are necessary, even overnight steps. Consequently, it is a sophisticated, time-consuming procedure, and harsh chemicals like peroxysulfuric acid are needed.

Alternating current (AC) electrokinetic (ACEK) effects, like dielectrophoresis (DEP), are a promising alternative for surface functionalization. DEP provides the benefits of

Abbreviations: ACEK, AC electrokinetic; ACEO, AC electroosmosis; BG, background; DEP, dielectrophoresis; ITO, indium tin oxide; ROI, region of interest; SAM, self-assembled monolayer.

being a rapid method with a low need of sample volume. No prior chemical modification either of the sensor surface or the bio-receptor is needed. Furthermore, the spatial control of functionalization is possible down to the nm-scale. DEP is the lateral force that acts on polarizable particles in an inhomogeneous electric field. As a result of this force effect, the polarizable particles move either towards (positive DEP [pDEP]) or away (negative DEP [nDEP]) from the area of high electric field strength. The dielectric force that acts on a spherical particle is given by

$$F_{DEP} = 2\pi\varepsilon_0\varepsilon_m r^3 Re\left[K(\omega)\right]\nabla|E|^2 \quad (1)$$

where r is the radius of the particle, $Re[K(\omega)]$ is the real part of the Clausius–Mossotti factor, and $|E|$ is the electric field strength. Thus, the dielectric force depends on the particle radius, the applied frequency, the polarizability of the particle and its surrounding medium, and on the gradient of the electric field, which in turn depends on the applied voltage, as well as on the geometry and sharpness of the electrodes. Particles can be accumulated, transported, separated, trapped, and characterized. Studies on the DEP manipulation of biological objects have progressed from the micrometer range like cells [2–5] and bacteria [6–9], to viruses [10–12], proteins [13, 14], DNA [15, 16], and even small molecules [17]. A commercial use has been demonstrated as well [18–21]. The decrease in object size has been possible due to improved fabrication technologies of nanometer-sized electrodes. As the dielectrophoretic force decreases with decreasing particle size (Equation 1) and the influence of Brownian motion and electrohydrodynamic effects on the particle is growing [22], higher field gradients are needed for the manipulation of smaller objects. Nanoelectrodes, like the ones presented in this paper, fulfill the generation of those required gradients.

ACEK forces, and especially DEP, undergo an increasing interest in the spatial manipulation of medically relevant sub-micrometer objects like exosomes [23], liposomes [24, 25], and organelles [26–28]. When it comes to the manipulation of viruses by DEP and related phenomena, different virus types have been investigated so far, like tobacco mosaic [11, 12, 29, 30], herpes simplex [10, 12, 31], Sendai [32, 33], influenza [34–37], hepatitis [38], norovirus [39], rotavirus [39, 40], adenovirus [40], Sindbis [41], and cowpea mosaic [29]. Although older studies are focused on the characterization of the dielectric behavior and the dielectric properties of the viruses, newer studies are more focused on the bioanalytical application and integration into a point-of-care system.

Usually, accumulation by DEP is a reversible process. There are only a few reports found in the literature on permanent immobilization by DEP in the sub-micrometer range. The first was Yamamoto et al. demonstrating the control over temporal or permanent immobilization of bovine serum albumin (BSA) by adjusting the electric field strength [42]. Furthermore, permanent immobilization of BSA [43], horseradish peroxidase [44], and polystyrene nanobeads [45] with the same electrode design as presented in this paper has been demonstrated previously. However, the degree of permanent immobilization of nanobeads turned out to be size dependent. To our knowledge, no reports of permanent immobilization of viral particles by DEP exist. It was an open question whether this would be possible, all the more the material properties and the structure of viruses significantly differ from those of polystyrene spheres and protein molecules. In terms of sizes, viruses are between cells and proteins. Although cells are biological objects whose electrokinetic behavior has been extensively investigated and is quite well understood, this is not the case for proteins [46]. Viruses are of biological origin; thus they are significantly more heterogeneous in their properties than nanobeads. For this study, the influenza virus has been chosen because of its paramount medical relevance. Its structure and composition are much more complex than nanobeads and proteins. Influenza viruses are spherical and enveloped particles with diameters between 80 and 120 nm. Their lipid membrane is covered with different proteins, mainly hemagglutinin and neuraminidase. Underneath this membrane lays a shell made of matrix proteins. Inside the viral particle are eight RNA segments embedded in nucleoprotein molecules. Thus, influenza viruses are inhomogeneous particles, consisting of different layers and molecules, each with different dielectric properties. A scheme of its structure and a scanning electron micrograph are shown in Figure 1.

Here we present the use of ACEK forces, like DEP, as a simple and fast method to immobilize influenza X-31 onto nanoelectrode arrays for bioanalytical applications. The accumulation of viral material over time is observed. Through the array design, comprising thousands of nanoelectrodes, each electrode can be considered a single event and allows a simultaneous statistically meaningful analysis. It was further investigated whether the immobilization is temporary or permanent. A detailed look at the spatial distribution by high-resolution fluorescence microscopy combined with deconvolution is demonstrated.

2 | EXPERIMENTAL SECTION

2.1 | Electrode configuration and preparation

The electrode chips—representing the core of the experimental setup—were produced by IHP GmbH in a

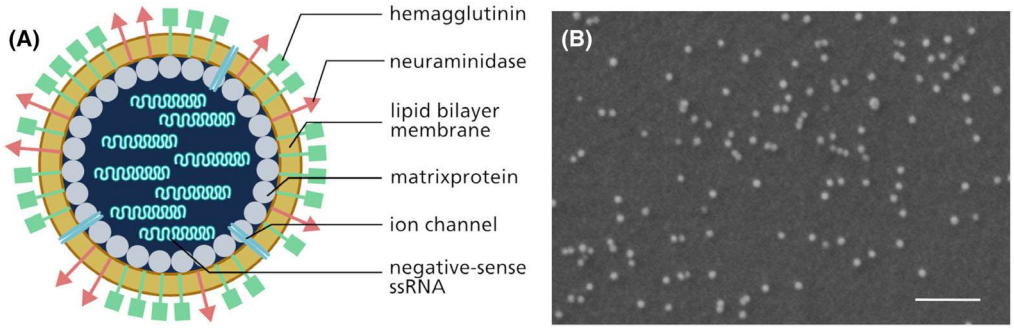

FIGURE 1 Structure and morphology of the influenza A virus. (A) Schematic illustration of the influenza virus. It is a spherical, enveloped virus. Its genome comprises eight negative-sense, single-stranded RNA segments. Based on the two surface proteins, hemagglutinin and neuraminidase, influenza viruses can be divided into subtypes. (B) Scanning electron micrograph showing single virus particles on a gold substrate. Scale bar = 1 µm [Color figure can be viewed at www.electrophoresis-journal.com]

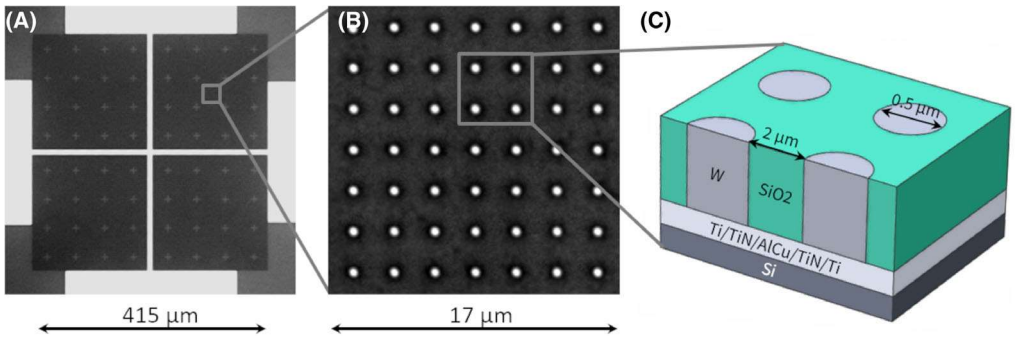

FIGURE 2 Electrode configuration. (A) Microscopic image of the four nanoelectrode subarrays. Each array is made up of 6256 electrodes. (B) Detailed view of (A) showing 49 electrodes. (C) Schematic cross-section of the electrode chip. The cylindrical electrodes are made up of tungsten with a diameter of 500 nm and a mutual distance of 2 µm. They are electrically connected by an underlying Ti/TiN/AlCu/TiN/Ti layer [Color figure can be viewed at www.electrophoresis-journal.com]

standard 250 nm CMOS protocol on 8 inch silicon wafers. The detailed fabrication process was described in [43, 47]. Single chips have an overall size of 1 cm × 1 cm. Four individual electrode arrays are located in the center of the chip (Figure 2A) allowing up to four experiments on the same chips or serving as an internal control. Each array is made up of 6256 tungsten electrode pins arranged in a "bed of nails" design, meaning the electrodes are evenly distributed in an 80 × 80 matrix with a mutual distance of 2 µm. For better orientation, 16 electrode-free, cross-shaped areas are integrated into each array. The individual electrodes are cylindrically shaped with a diameter of 500 nm (Figure 2C) and are embedded in SiO_2. An underlying conductive Ti/TiN/AlCu/TiN/Ti layer electrically connects all electrodes within one subarray, whereas the subarrays stay electrically separated from each other.

The chip was mounted onto a microscope slide. A sample chamber was prepared by punching a 3 mm hole into an 80 µm thick lamination foil and hot-melting this foil onto the electrode chip at around 80°C. This foil also served as a spacer to separate the electrodes from the counter electrode. For the latter, a cover slip coated with indium tin oxide (ITO; 70–100 Ω) was used (SPI Supplies; 06462-AB). Its transparency allowed observing the experiment by optical microscopy in real-time. An extra pad covered with copper tape was used to close the electrical circuit between the electrodes and the ITO cover slip. Copper wires were attached to the contact pads by conductive silver paint (Conrad; 530042) and were soldered to the connector. A schematic scheme of a prepared chip is presented in Figure 3A.

2.2 | Experimental setup

The AC signal was generated by a function generator (Wavetek; Model 193) and further amplified by a wideband amplifier (Toellner; TOE 7606). The attenuator prevented the wideband amplifier from being overdriven by the output signal of the function generator. This ensured that the voltage maintained its sine shape. The

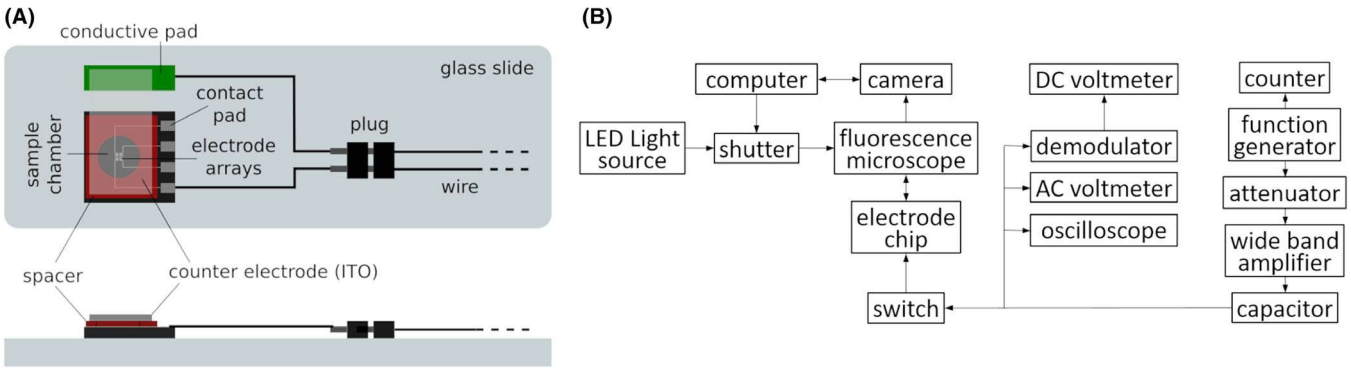

FIGURE 3 Scheme of: (A) The top and side view of a prepared electrode chip. The chip was taped onto a microscope slide. An ITO cover slip served as the counter electrode and was electrically contacted by a pad covered with copper tape (green). The electrodes and the ITO cover slip were separated by an 80 µm thick spacer (red). A 3 mm wide hole punched into the spacer formed the sample chamber. (B) The electrical and optical setup. An AC signal was generated by a function generator and amplified by a wideband amplifier. A frequency counter, voltmeters, and an oscilloscope were used to monitor the frequency and the amplitude. Images were acquired by a fluorescence microscope equipped with a CCD camera. CCD, charge-coupled device; ITO, indium tin oxide [Color figure can be viewed at www.electrophoresis-journal.com]

frequency was monitored by a separate frequency counter (Conrad; Voltcraft 7202) and the amplitude was observed with an oscilloscope (Hameg; HM307), an AC voltmeter (Uni-Trend; UT803), and a DC voltmeter (Mastech; M9803R) equipped with a demodulator probe (Testec; TT-DE 112). A mechanical switch was used to turn on or off the AC signal. A 3.3 µF capacitor (WIMA; MKC4 SV21) prevented any DC signal from reaching the electrodes. All devices were connected by coaxial cables except for the two-wire cable between the switch and electrode chip. A scheme of the electrical setup is shown in Figure 3B.

To monitor the experiments, an upright fluorescence microscope (Olympus; BX51) equipped with a cooled charge-coupled device camera (Olympus; F-View II) was used. Fluorescence images were acquired using a 60× objective (Olympus; LUCPlanFLN; NA 0.70) or a 100× objective (Olympus; MPlanFLN; NA 0.90) and a Cy5 filter set (AHF; F46-006; excitation: ET620/60, emission: ET700/75, beam splitter: T660lpxr). An LED lamp (CoolLED; pE-4000) served as the illumination source combining a 365 nm LED, a 460 nm LED, a 525 nm LED, and a 635 nm LED with an intensity setting of 5% for bright field images and a setting of 100% for fluorescence images. The exposure time, the shutter, the shutter driver (Uniblitz; Model VCM-D1), and image acquisition were controlled by the software Cell^{M} (Olympus; Version 3.1).

Images were processed using the software ImageJ (version 1.53a or higher) extended with the plugins *MicroArray Profile* (OptiNav Inc., USA), *Diffraction PSF 3D* (OptiNav Inc., USA), and *DeconvolutionLab* (Biomedical Imaging Group, EPFL, Switzerland). OriginPro2019 (Version 9.6.0.172) was used for curve fitting.

2.3 | Experimental procedure

The viral material (Influenza A/Aichi/2/68 H3N2, short X-31) was provided by the Robert Koch-Institute in Berlin. The virus sample was prepared from allantoic fluid of hen eggs and purified and concentrated by density-gradient centrifugation. Then it was inactivated by β-propiolactone.

The initial protein concentration of 141 µg/ml was determined by BCA assay and it was stored in PBS-buffer at −80 °C. The virus sample was covalently labeled with the fluorophore DY-634 by coupling via a reactive NHS-ester to the lysine groups of the viral proteins (empBiotech; MK-D0107). Ultrafiltration spin columns (Sartorius; Vivaspin 500; 30 000 MWCO; VS0121) were used to remove the unbound dye and to exchange the buffer against ultrapure water. After four centrifugation cycles (5 min, 16 100 *g*), the virus sample had a protein concentration of around 80 µg/ml.

As the amount of virus sample was in the µl range and electrical conductivity is a critical parameter in electrokinetic experiments, a purpose-built conductivity probe, consisting of four platinum wires (0.1 mm diameter) attached to the inside of a 200 µl pipette tip, was constructed. This four-electrode arrangement allowed minimal electrode polarization despite the small electrode surface. Conductance was measured by an LCR-meter (HIOKI 3532–50; 1 kHz; 1 V) in the four-terminal sensing mode. The setup was calibrated by a series of KCl solutions from 2 to 4000 µS/cm in logarithmic steps against a conductometer (WTW Cond 197i) equipped with a conductivity probe (WTW TetraCon® 325). The benefit of the purpose-built setup compared to the conductometer

is its small measurement volume from 20 µl down to 8 µl. Finally, the conductivity of the labeled and desalted virus sample was determined to a value of 3 µS/cm. Changes due to contamination from the ITO or the electrode chip have not been monitored but have been kept as small as possible by rinsing both with ultrapure water before the experiment and by drying with an N_2 stream. To keep the conductivity low, any further dilution of the dyed virus sample was done in ultrapure water.

For ACEK experiments, 5 µl of a 1:20 diluted solution of stained viral material was loaded into the sample chamber of the prepared electrode chip. The sample was covered with the ITO cover slip and an AC signal of 10–20 kHz and 3.5 V_{rms} was applied.

3 | RESULTS AND DISCUSSION

3.1 | Temporal development of the dielectrophoretic immobilization

3.1.1 | Definition of experimental parameters

To maximize immobilization efficiency, the applied frequency was systematically investigated from 10 to 20 kHz. Based on previous publications, this is a valid frequency range to immobilize sub-micrometer objects like nanospheres and macromolecules [17, 43–45]. Frequencies below 5 kHz promote the formation of bubbles due to electrolysis [22, 44, 48], whereas high frequencies lead to electrothermal fluid flow [49]. Although the viral material had a rather clumpy and uneven accumulation at the electrodes at 10 and 15 kHz (not shown), it was possible to reach a more even distribution at 20 kHz. Therefore, all experiments were performed at 20 kHz.

High voltages are undesired because they promote side effects like electrolysis, joule heating, and fluid streaming, which in turn counteract the dielectrophoretic force [22, 47–49]. A voltage of 3.5 V_{rms} was chosen to keep these side effects low, whilst reaching a fast but gentile immobilization and to overcome Brownian motion.

The dielectric immobilization of the X-31-virus was monitored by fluorescence microscopy. Images were acquired with a 60× objective and a Cy5 filter set at an exposure time of 500 ms. Images were acquired every 20 s for a total timespan of 180 s. The shutter was closed between image acquisition to minimize bleaching effects. Thus, $t = 0$ s was the only point in time when no AC-electric field was applied.

A non-activated array on the same chip was used as a negative control. During the experiment, no viral material accumulated on the non-activated electrodes. This demonstrates that the viral material was not immobilized by adsorption to the activated electrodes but has been drawn to the electrodes by DEP in a controlled manner.

3.1.2 | Definition of ROI size

For image evaluation, different regions of interest (ROI) have been investigated: three circular and two ring-shaped. With a pixel size of 147.5 nm × 147.5 nm, the circular ROIs had diameters from about the electrode size with 4 px (C4, d = 590 nm), to 8 px (C8, d = 1.18 µm), and finally 16 px covering almost all the area halfway to the neighboring electrodes (C16, d = 2.36 µm). Furthermore, two ring-shaped ROIs were defined with an outer diameter of 8 px (R8) and 16 px (R16) and an inner diameter of 4 and 8 px, respectively, thus covering only the area around the electrodes. All ROI sizes were concentrically aligned as shown in Figure 4A. A rectangular ROI, comprising an area of 12 × 7 electrodes at the corner of the diagonally opposite unused electrode array, was defined as the ROI for background (BG) determination. The BG signal was determined for each time point to take into account the change in virus concentration with time and thus the changing BG fluorescence in the volume. Finally, the mean and integrated intensity of 30 electrodes of the outermost row (row 1) have been plotted for all ROI sizes (Figure 4). The increase of the amount of immobilized viral material with duration time shows an exponential correlation for all investigated ROIs:

$$y = y_0 + A_1 e^{\frac{-t}{t_1}} \tag{2}$$

with R^2 from 0.98 to 0.99. The graphs are monotonically increasing with y_0 as the asymptote. The tangent in $t_0 = 0$ intersects the asymptote y_0 at t_1. The function value at this point is around 63% of the limit; thus, $y(t_1) = 0.63y_0$. At t_1, 63% of the maximum intensity is reached. Consequently, the smaller t_1, the faster and stronger the increase of the mean fluorescence intensity for the corresponding ROI. A strong increase of mean fluorescence intensity exists for all ROIs up to 60 s (Figure 4A). The focus of attraction is located at the electrodes themselves as demonstrated by C4 and its small t_1 value. It is the area to which the viral material is first drawn to. Here, a plateau is reached after 80 s, showing that saturation is reached. There are four possible explanations for this saturation. (i) The viral material in the volume has been depleted. A hypothesis that is easy to refute. The lasting increase of intensity for C8 and C16 from 80 s and the increasing intensity up to 180 s for the electrodes in rows 2–4 (Figure 5E) demonstrate that there was still a supply of viral material. (ii) Inspection of Equation (1) demonstrates that the DEP force depends on the

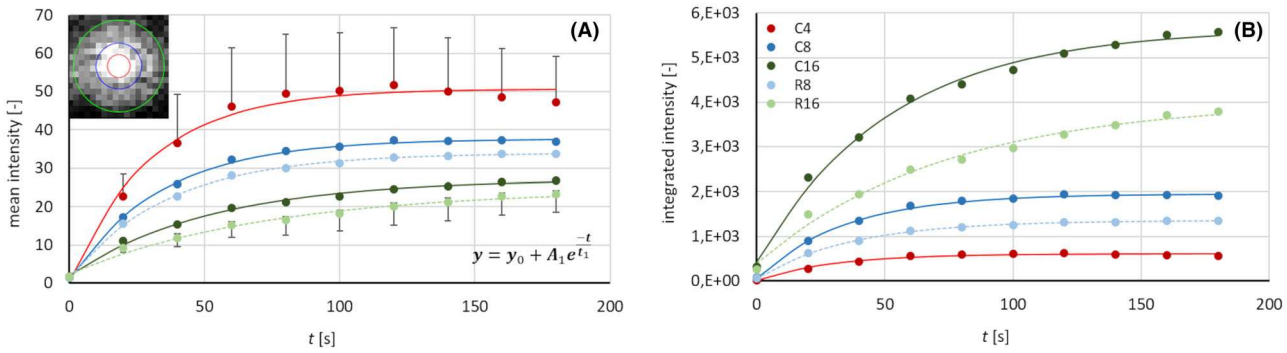

FIGURE 4 Dependence of the mean (A) and integrated (B) fluorescence intensity for different ROIs on the duration of the applied AC field. An AC field with $f = 20$ kHz and $U = 3.5$ V_{rms} was applied for 180 s. Three circular ROIs (solid lines) with a diameter of 4 px (C4), 8 px (C8) and 16 px (C16) were defined, as well as two ring-shaped ROIs (dashed lines) with an outer diameter of 8 px (R8) and 16 px (R16) and an inner diameter of 4 and 8 px, respectively. All ROIs were concentrically aligned (shown in the upper left corner). Overall, 30 electrodes from the outermost row (row 1) have been evaluated. All values are BG-corrected, 1 px = 147.5 nm × 147.5 nm. (A) Mean fluorescence intensity (dots: data; lines: exponential curve fit with Equation (2); C4: $y_0 = 50.6$, $A_1 = -49.9$, $t_1 = 29.9$, $R^2 = 0.98$; C8: $y_0 = 37.7$, $A_1 = -36.3$, $t_1 = 34.1$, $R^2 = 0.99$; C16: $y_0 = 27.2$, $A_1 = -25.1$, $t_1 = 52.2$, $R^2 = 0.99$; R8: $y_0 = 33.9$, $A_1 = -32.3$, $t_1 = 36.7$, $R^2 = 0.99$; R16: $y_0 = 24.6$, $A_1 = -22.2$, $t_1 = 73.3$, $R^2 = 0.99$). Error bars show standard deviation and are displayed only for the top and bottom curve. (B) Integrated fluorescence intensity. Gray values of all pixels within one ROI have been summed up (dots: data; lines: exponential curve fit as in A; C4: $y_0 = 607.7$, $A_1 = -599.4$, $t_1 = 29.9$, $R^2 = 0.98$; C8: $y_0 = 1957.9$, $A_1 = -1887.5$, $t_1 = 34.1$, $R^2 = 0.99$; C16: $y_0 = 5651.7$, $A_1 = -5211.0$, $t_1 = 52.2$, $R^2 = 0.99$; R8: $y_0 = 1355.4$, $A_1 = -1290.7$, $t_1 = 36.7$, $R^2 = 0.99$; R16: $y_0 = 4036.5$, $A_1 = -3637.6$, $t_1 = 73.3$, $R^2 = 0.99$). AC, alternating current; BG, background; ROI, region of interest [Color figure can be viewed at www.electrophoresis-journal.com]

gradient of the electric field-squared $\nabla|E|^2$. The electric field strength and the gradient are strongest at the electrode edge but decay very quickly with distance. Because of a relatively large distance between electrode array and counter electrode, in most of the volume above the electrode chip, the electric field is homogeneous, that is, the electric field lines run parallel to each other and orthogonal to the chip surface. Here, no dielectric force acts on the viral material. Thus, there is a height limitation, to which the viruses experience a substantial dielectric force. Electric-field plots of the cylindrical electrodes have been published previously [47]. (iii) The insulating character of the immobilized viral material shields the electric field. The larger the layer thickness, the greater the shielding. Thus, there is a further limitation for the amount of material that can be immobilized. (iv) Last but not least, the mere presence of viral material after the initial course of attraction and immobilization hinders further accumulation; hence, fluorescence intensity increases.

Due to the optical resolution of around 550 nm for the 60× objective combined with the Cy5 filter-set, it is not possible to differentiate whether the material is drawn to the edge of the electrodes or to the surface of the electrodes. This aspect will be discussed in more detail later (Section 3.3).

From 80 to 140 s, the mean intensity is fluctuating around a value of 50% ± 2% for C4. From 140 to 180 s, the mean intensity decreases by 5.8%, probably due to bleaching or self-quenching. C8 is reaching a plateau at 120 s. From there, the signal is fluctuating around a value of 37% ± 0.5%. C16 is increasing up to 160 s and reaching a plateau. This demonstrates that after saturation at the electrodes, the viral material collects more and more in the space between. To include this viral material in further analysis, a circular ROI with a diameter of 16 px was chosen.

3.1.3 | Immobilization of viral material and side effects

Figure 5 shows the intensity time traces of 30 electrodes for rows 1–7 each. A gradient in fluorescence intensity and thus in the amount of immobilized viral material exists starting from the outermost row to the inner ones. This effect has also been observed for the dielectric immobilization of BSA [43] and polystyrene nanobeads [45]. This gradient is caused by several forces acting simultaneously.

In an AC-electric field, DEP is not the only force acting on a polarizable particle. Such a particle undergoes a sum of forces like sedimentation, Brownian motion, DEP force, and other electrohydrodynamic forces, like AC electroosmosis (ACEO), and electrothermal fluid flow. The later ones have been reported to be able to generate a fluid flow across electrodes [50–55]. For ACEO, the fluid motion is caused by the tangential part of the electric field that exerts a coulomb force on the counterions of the induced electric double layer at the electrode–electrolyte interface. On the other hand, power dissipation close to the electrodes

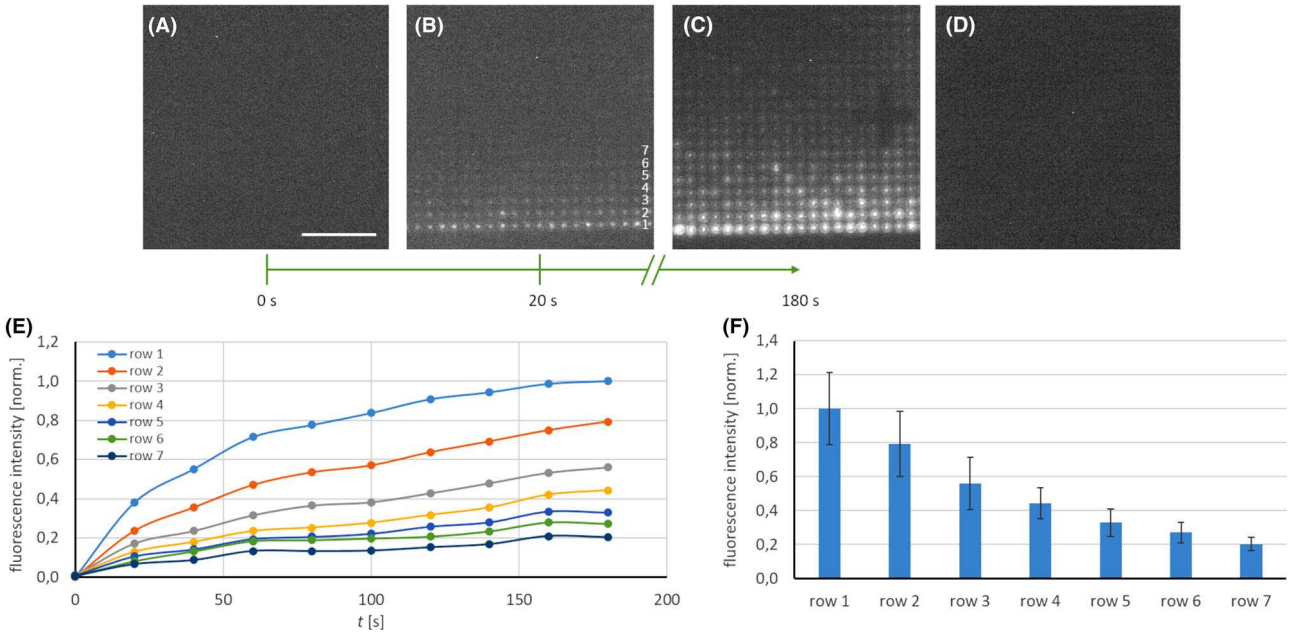

FIGURE 5 Temporal development of the dielectric immobilization of influenza viruses over a period of 180 s at 20 kHz and 3.5 V_{rms}, at timepoints of 0 s (A), 20 s (B), and 180 s (C). A non-activated array on the same chip was used as a negative control (D). (A–D) Fluorescence images: 60× objective, Cy5 filter, exposure time = 500 ms, scale bar = 15 µm. Row numbers are depicted in (B). (E) and (F) Background corrected, normalized fluorescence intensities of 30 electrodes in rows 1–7 each. Temporal development from 0 to 180 s (E) and dependence of intensity on row number at t = 180 s (F) [Color figure can be viewed at www.electrophoresis-journal.com]

causes a thermal gradient in the volume. This leads to buoyancy forces as well as gradients in conductivity and permittivity and thus to electrothermal fluid flow. The sum of these effects acts on the viral material and therefore it is rather an electrokinetic manipulation than a manipulation by DEP alone.

The electrohydrodynamic forces produce a vortex-shaped fluid motion at all four edges of the activated array. At each edge, the fluid moves from outside the array toward its edge, then sweeps across the outer rows of electrodes toward the array's center, and then streams upward and back into the volume. A viscous drag force on the viral material arises from this fluid flow. For a spherical particle, the drag force is given by Stoke's law:

$$F_{drag} = 6\pi\eta r v \tag{3}$$

where η is the viscosity of the fluid, r is the particle radius, and v is the particle velocity [56]. As the DEP force is proportional to the particle volume (Equation 1), that is, to the radius' cube, the drag force is directly proportional to the radius (Equation 3). The DEP force decreases faster with decreasing particle size than the drag force. Consequently, here, the drag force has a stronger impact on the movement of the viral material than it does on common DEP-manipulated objects like mammalian cells or bacteria.

Furthermore, field simulations from [43] demonstrate that the gradient $\nabla|E|^2$ is strongest at the corner and outer row electrodes (row 1). Consequently, depending on the spatial position of the viral material, either the DEP force or the drag force is dominant. Viral material that is drawn to the electrodes starts to stack up. The height of the stack (and thus the fluorescence intensity) depends on the strength of the DEP force or $\nabla|E|^2$ and on the strength of the competing drag force. The temporal progression of the immobilization shows an exponential correlation (Equation 2) for all investigated rows with R^2 from 0.94 to 0.99. Due to the strong gradient $\nabla|E|^2$, there is strong immobilization in row 1 until a plateau is reached. The explanation of this plateau formation is in-line with the explanation from Section 3.1.2. Because of the decrease of $\nabla|E|^2$ with an increasing row number, the time constant t_1 is increasing from 51.9 s at the first row to 85.2 s, 108.9 s, and 187.1 s for rows 2–4, respectively. The continuous rise in fluorescence intensity up to 180 s for rows 2–4 demonstrates a steady supply of viral material from the sample volume. From row 5 on, the competition between DEP force and drag force becomes clear. These rows show an early plateau formation and the intensity at 180 s amounts to less than 30% of row 1. Here, viral material is still immobilized by DEP, but because of the weaker $\nabla|E|^2$ and increasing drag force, the amount of viral material is lower. The endpoint fluorescence intensity in Figure 5F shows a good correlation to the simulated values of $\nabla|E|^2$ and the height profiles of immobilized BSA from [43]. Furthermore, the vortex-shaped fluid flow at all four edges of the activated array

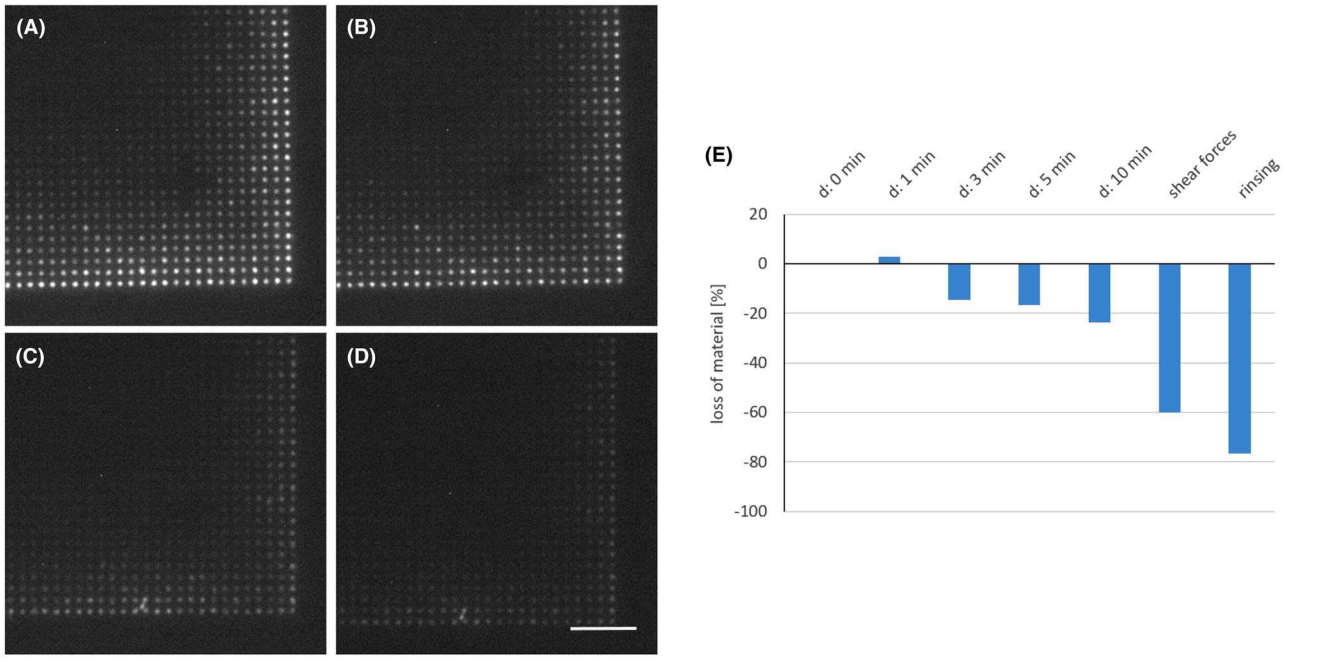

FIGURE 6 Fluorescence images acquired directly after switching off the electric field (A), after a dwell time of 10 min of diffusion (B), after applying shear forces by lifting up and putting back down the ITO cover slip (C), and after rinsing with ultrapure water (D). 60× objective, Cy5 filter, exposure time = 500 ms, scale bar = 15 µm. (E) Relative loss of viral material compared to the starting point (a dwell time of 0 min). *d*, dwell time. ITO, indium tin oxide [Color figure can be viewed at www.electrophoresis-journal.com]

prevents any viral material to come in close proximity to the electrodes in the central part of the array.

3.2 | Temporary versus permanent immobilization

Investigating the literature for the immobilization of viral material via pDEP, it has always been a reversible process, meaning by switching off the field and rinsing the chip, the viral material was removed from the electrodes. Here, the influence of diffusion, shear forces, and rinsing on the stability of the immobilization has been investigated.

Image acquisition has been done with the 60× objective, Cy5 filter set, and an exposure time of 500 ms. After the accumulation of viral material for 180 s, the electric field was switched off and the fluorescence signal was measured after a dwell time of 0, 3, 5, and 10 min (diffusion). To deliberately produce shear forces, the ITO-cover glass was gently lifted with a pair of tweezers and put back onto the chip. In the last step, the chip was rinsed with ultrapure water and blown dry with N_2 (Figure 6A–D).

The BG was determined for an area of 9 × 7 electrodes at the corner of the diagonally opposite unused array and subtracted for each image separately. For image evaluation, a rectangular ROI comprising an area of 9 × 17 functionalized electrodes was defined and the integrated intensity for each BG-corrected image was measured. Then, the relative loss compared to the starting point (a dwell time of 0 min) was determined (Figure 6E).

The time $t = 0$ min corresponds to the moment immediately after switching off the electrical field and is defined as the starting point for all further states. It is to be expected that more and more material will diffuse away from the electrodes over time and thus the signal will decrease. This is the case for a dwell time of 3, 5, and 10 min. After 10 min, there is already a loss of approx. 24%. The situation is different at a dwell time of 1 min, where an increase of 2.8% was measured. Possible explanations for this observation are as follows: (i) The fluid streaming does not stop simultaneously with switching-off of the electric field. Thus, new viral material was transported from the volume into the evaluated ROI area giving a rise in fluorescence signal. (ii) At high concentration, many fluorescence dyes form dimers leading to a self-quenching effect. For fluorescent dyes from Dyomics, this effect has been used to develop DNA probes labeled with the same dye at both ends [57, 58]. Here, the immobilized viral material is so tightly packed that the spatial distance between the fluorophore molecules might be so small that they quench each other. (iii) The high concentration of fluorophore molecules may also lead to a self-absorption of the emitted photons.

Lifting and putting back the ITO cover slip let the air–fluid interface run twice across the electrode arrays and the immobilized viral material. The resulting shear forces lead to a material loss of around 60%. Finally, rinsing the

chip with ultrapure water leads to a total loss of material of around 77%.

The remaining, permanently immobilized material sticks to the tungsten electrodes. The reason for the permanent immobilization is not clear. Presumably, the attracted viral material displaces the hydration layer at the electrodes surface. Consequently, hydrophobic interactions and van der Waals forces between viral surface proteins and electrodes emerge. So far, it has been demonstrated that this permanent immobilization depends on the electric field strength [42] and the size of the immobilized object [45].

3.3 | Spatial distribution of viral material on the electrodes

Due to scattering and diffraction of light, fluorescence images include considerable out-of-focus light originating from regions above and below the focal plane. As a result, fluorescence images are blurred and the resolution is reduced. Image deconvolution uses information describing the source of light distortion and thus seeks to remove or to reassign the out-of-focus light to its point of origin. Consequently, it is a method to improve image contrast, resolution, and signal-to-noise ratio. There is a wide range of applications for the deconvolution of fluorescence images, like colocalization analysis [59], structural investigation of the actin cytoskeleton of yeast [60], and the detection of single RNA molecules [61]. The result depends on the parameter settings, the image to be processed, and the chosen algorithm. The optical distortion is defined by a point spread function (PSF). Sage et al. have compared different deconvolution algorithms of the plugin *DeconvolutionLab2* for ImageJ. Although naive inverse filtering (NIF) produces severe artifacts and Tikhonov regularization (TR) and regularized inverse filtering (RIF) produce ringing artifacts, best results have been reported from iterative algorithms like Landweber (LW), Richardson–Lucy (RL), and Tikhonov–Miller (TM) [62].

Following the immobilization, the chip was rinsed with ultrapure water and blow-dried with N_2. Fluorescence images of the lower right corner have been acquired with a 100× objective, a Cy5 filter, and an exposure time of 5 s (Figure 7A). The PSF was generated via the ImageJ plugin *Diffraction PSF 3D* (NA 0.9, $\lambda = 664$ nm, image pixel spacing = 86 nm). The ImageJ plugin *DeconvolutionLab* was used with the RL algorithm (number of iterations = 100). In order to better fit the rectangular pixel distribution to the circular electrodes, the deconvolved image was resized via ImageJ by a factor of 8 applying bilinear interpolation; thus one pixel of the original image now is blown up to a size of 8 px × 8 px.

For an area of 7 × 17 electrodes, a grid of ROIs was created using the plugin *MicroArray Profile*. With the help of a self-written macro (ImageJ Macro language), the coordinates of the grid were read out and transformed into rectangular ROIs of the same size (Figure 7B). These ROIs were used to cut out each of the 119 electrodes into single images. Finally, pixels at the same position for all 119 images were summed up. The projection of the summation is shown in Figure 7C.

Image evaluation by the 100× objective combined with deconvolution reveals an individual distribution of viral material (Figure 7B). Thus, each electrode can be considered a single event. Although at some electrodes the viral material shows a ring-shaped or nearly ring-shaped accumulation, at other electrodes the accumulation is not clear. The summation projection combines those single events and reveals an accumulation preferentially at the electrode edge forming the ring-shaped appearance.

The normalized mean fluorescence intensity, integrated over a set of concentric rings, as a function of distance from the electrode center is plotted in Figure 7F. Accordingly, 31 ring-shaped ROIs with an outer radius starting from 2 px (21.5 nm) to 62 px (666.5 nm) and a ring width of 2 px have been concentrically aligned on top of the summation projection. The mean fluorescence intensity of the entire area outside the outermost ring was defined as the BG. The same has been done with the summation projection of 70 empty electrodes from the center of the same array (not shown). The mean fluorescence intensity for each ring was measured, the BG was subtracted as well as the mean fluorescence intensity of the empty electrodes, and finally values were normalized.

The graph starts at the electrode center and runs outward up to a distance of 666.5 nm. The red line marks the position of the electrode edge. The ring-shaped summation projection (Figure 7C) and the plot (Figure 7F) are in-line with theory and field simulations [43, 47] where field gradient and thus DEP force is strongest at the edge of the electrodes. Due to the bending of the electric field at the edge of the electrode, the location of the greatest electric field strength is not at a 90° angle on top of the edge but displaced diagonally outward to it. Thus, the fluorescence peak is shifted outward by 50 nm from the edge. The fluorescence decreases with increasing distance down to zero at a distance of approx. 450 nm from the electrode edge. In comparison, the intensity remains at a share of 50% at the electrode center. Although so far ACEO has been used to explain the fluid flow in the volume above an activated array, it can also be adduced to explain the attraction of viral material onto the electrode surface, where the electric field gradient is significantly smaller. The tangential part of the electric field points radially from the edge to the electrode center and thus draws the viral material across

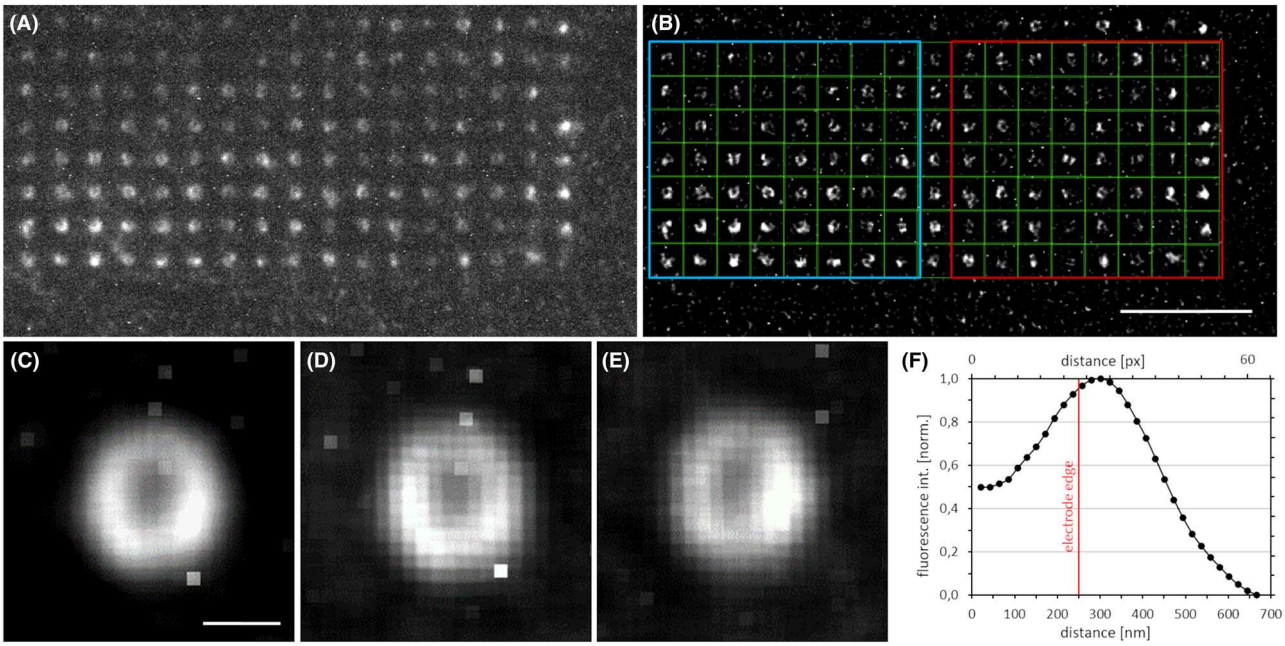

FIGURE 7 (A) Fluorescence image of the lower right corner of the electrode array: 100× objective, Cy5 filter, exposure time = 5 s. The image has been deconvolved via ImageJ and enlarged by a factor of 8 and bilinear interpolation (B). Same-sized ROIs for 119 electrodes have been defined (green), cut into single images, and then summed up to the summation projection (C). (D) and (E) are the summation projection of the blue and red areas from (B), respectively. (F) Normalized mean fluorescence intensity as a function of distance for (C). The *x*-axis starts at the electrode center. The red line marks the electrode edge. Scale bar from (B) = 10 µm, scale bar from (C) = 500 nm. ROI, region of interest [Color figure can be viewed at www.electrophoresis-journal.com]

the surface. This effect has been used to focus spores, latex beads, and yeast cells in a controlled manner at the surface center of electrodes [63]. This is another indication that the immobilization of viral material occurs through the combination of several electrokinetic effects.

The summation projections from Figure 7D and E demonstrate the influence of the global fluid flow on the spatial distribution of the immobilized viral material. The 64 electrodes in the blue area (Figure 7B) were exposed to a fluid flow streaming from beneath the array across the outer rows of electrodes, resulting in a pronounced accumulation at the bottom half of the summation projection (Figure 7D). Electrodes in the red area are located in the lower right corner of the array. Thus, they are exposed to fluid streaming from beneath as well as from the right, resulting in a pronounced accumulation on the bottom right side of the summation projection (Figure 7E).

4 | CONCLUDING REMARKS

The electrically controlled immobilization of the influenza virus strain X-31 onto nanoelectrodes has been demonstrated. Although DEP and ACEO are the dominant forces for the accumulation, electrothermal fluid flow among others is the dominant force for the emerging intensity gradient. The combination of fluorescence microscopy and image processing by deconvolution provided a suitable approach to determine the spatial distribution of the accumulated viral material. The most outstanding feature of our experimental setup and design is the permanent immobilization without the need of prior chemical modification of the surface or the bio-receptor. Thus, subsequent handling independently from the electrical setup is possible. Further experiments are necessary in order to better understand the interactions between surface proteins and electrodes. Changing the surface proteins or the medium is expected to have an influence on the van der Waals forces. Thus, comparative experiments with changed surface proteins by, for example, protein digestion or crosslinking as well as change of the pH value, ionic concentration, or ionic composition of the medium might be suitable. The presented platform allows a wide range of applications: (i) as an immune assay to detect antibodies in sera or to determine antibody titer. (ii) The four electrode arrays can be functionalized individually, allowing a multiparameter measurement. Thus, the characterization of influenza subtypes or different viruses like the corona virus is possible. (iii) Singling of polystyrene nanobeads has been demonstrated by Knigge et al. [45]. An electrode diameter half the size of the immobilized object is needed. Thus, a single virus particle analysis should be possible

with an electrode diameter of 50 nm. This is supported by the array design, where thousands of electrodes allow a statistical evaluation,and each electrode stands for a single experiment (Figures 4 and 5). The regular arrangement of the electrodes favors an automated evaluation. (iv) A fixation method for structural analysis by super-resolution microscopy. (v) By optimizing the experimental parameters, a better separation of DEP and ACEO might be possible. Thus, the same electrode could be successively functionalized by two different objects. Here, DEP is used for the accumulation of object (a) at the rim and ACEO for the accumulation of object (b) on the surface. (vi) Each electrode can be used as part of an on-chip resonant circuit, whose frequency changes with a surface coverage of the electrode and, hence, serves as a measure of the amount of viruses attached to the electrodes [64, 65]. So in the future, the evaluation by fluorescence microscopy can be changed to an electrical evaluation. Thus, combined with microfluidics, this chip has the potential for a small and rapid point-of-care system.

ACKNOWLEDGMENTS

We thank the Robert Koch-Institute, Berlin, Dr. Wolff for providing us with X-31 samples. Financial support by the European Regional Development Fund (ERDF) and by The Brandenburg Ministry of Sciences, Research, and Cultural Affairs (MWFK) within the framework StaF (BioBic, 85004117) is gratefully acknowledged. We also thank the German Research Foundation (DFG) for funding by the Priority program Essence (SPP1857, HO1298/4-1). Sandra Stanke is supported by the German Academic Scholarship Foundation.

CONFLICT OF INTEREST

The authors have declared no conflict of interest.

DATA AVAILABILITY STATEMENT

Research data are not shared.

ORCID

Sandra Stanke https://orcid.org/0000-0003-3627-6706
Christian Wenger https://orcid.org/0000-0003-3698-2635
Ralph Hölzel https://orcid.org/0000-0002-0529-9174

REFERENCES

1. Vericat C, Vela ME, Benitez G, Carro P, Salvarezza RC. Self-assembled monolayers of thiols and dithiols on gold: new challenges for a well-known system. Chem Soc Rev. 2010;39:1805–34.
2. Keim K, Rashed MZ, Kilchenmann SC, Delattre A, Gonçalves AF, Éry P, et al. On-chip technology for single-cell arraying, electrorotation-based analysis and selective release. Electrophoresis. 2019;40:1830–8.
3. Li M, Anand RK. High-throughput selective capture of single circulating tumor cells by dielectrophoresis at a wireless electrode array. J Am Chem Soc. 2017;139:8950–9.
4. Thomas RSW, Mitchell PD, Oreffo ROC, Morgan H, Green NG. Image-based sorting and negative dielectrophoresis for high purity cell and particle separation. Electrophoresis. 2019;40:2718–27.
5. Waheed W, Alazzam A, Mathew B, Christoforou N, Abu-Nada E. Lateral fluid flow fractionation using dielectrophoresis (LFFF-DEP) for size-independent, label-free isolation of circulating tumor cells. J Chromatogr B: Analyt Technol Biomed Life Sci. 2018;1087–8:133–7.
6. Hamada R, Takayama H, Shonishi Y, Mao L, Nakano M, Suehiro J. A rapid bacteria detection technique utilizing impedance measurement combined with positive and negative dielectrophoresis. Sens Actuators, B. 2013;181:439–45.
7. Markx GH, Dyda PA, Pethig R. Dielectrophoretic separation of bacteria using a conductivity gradient. J Biotechnol. 1996;51:175–80.
8. Sanchis A, Brown AP, Sancho M, Martínez G, Sebastián JL, Muñoz S, et al. Dielectric characterization of bacterial cells using dielectrophoresis. Bioelectromagnetics. 2007;28:393–401.
9. Zhou R, Wang P, Chang H-C. Bacteria capture, concentration and detection by alternating current dielectrophoresis and self-assembly of dispersed single-wall carbon nanotubes. Electrophoresis. 2006;27:1376–85.
10. Hughes MP, Morgan H, Rixon FJ. Measuring the dielectric properties of herpes simplex virus type 1 virions with dielectrophoresis. Biochim Biophys Acta. 2002;1571:1–8.
11. Morgan H, Green NG. Dielectrophoretic manipulation of rod-shaped viral particles. J Electrostat. 1997;42:279–93.
12. Morgan H, Hughes MP, Green NG. Separation of submicron bioparticles by dielectrophoresis. Biophys J. 1999;77:516–25.
13. Washizu M, Suzuki S, Kurosawa O, Nishizaka T, Shinohara T. Molecular dielectrophoresis of biopolymers. IEEE Trans Ind Appl. 1994;30:835–43.
14. Hölzel R, Calander N, Chiragwandi Z, Willander M, Bier FF. Trapping single molecules by dielectrophoresis. Phys Rev Lett. 2005;95:128102.
15. Germishuizen WA, Wälti C, Wirtz R, Johnston MB, Pepper M, Davies AG, et al. Selective dielectrophoretic manipulation of surface-immobilized DNA molecules. Nanotechnology. 2003;14:896–902.
16. Hölzel R, Bier FF. Dielectrophoretic manipulation of DNA. IEEE Proc Nanobiotechnol. 2003;150:47–53.
17. Laux E-M, Wenger C, Bier FF, Hölzel R. AC electrokinetic immobilization of organic dye molecules. Anal Bioanal Chem. 2020;412:3859–70.
18. Hamada R, Suehiro J, Nakano M, Kikutani T, Konishi K. Development of rapid oral bacteria detection apparatus based on dielectrophoretic impedance measurement method. IET Nanobiotechnol. 2011;5:25–31.
19. Hoettges KF, Henslee EA, Torcal Serrano RM, Jabr RI, Abdallat RG, Beale AD, et al. Ten—Second electrophysiology: evaluation of the 3DEP platform for high-speed, high-accuracy cell analysis. Sci Rep. 2019;9:19153.
20. Gupta V, Jafferji I, Garza M, Melnikova VO, Hasegawa DK, Pethig R, et al. ApoStream (™), a new dielectrophoretic device

for antibody independent isolation and recovery of viable cancer cells from blood. Biomicrofluidics. 2012;6:24133.
21. Di Trapani M, Manaresi N, Medoro G. DEPArray™ system: an automatic image–based sorter for isolation of pure circulating tumor cells. Cytometry A. 2018;93:1260–6.
22. Castellanos A, Ramos A, González A, Green NG, Morgan H. Electrohydrodynamics and dielectrophoresis in microsystems: scaling laws. J Phys D: Appl Phys. 2003;36:2584–97.
23. Ibsen SD, Wright J, Lewis JM, Kim S, Ko S-Y, Ong J, et al. Rapid isolation and detection of exosomes and associated biomarkers from plasma. ACS Nano. 2017;11:6641–51.
24. Ibsen S, Sonnenberg A, Schutt C, Mukthavaram R, Yeh Y, Ortac I, et al. Recovery of drug delivery nanoparticles from human plasma using an electrokinetic platform technology. Small. 2015;11:5088–96.
25. Serafetinides AA, Makropoulou M, Spyratou E. In: Dreischuh TN, Daskalova AT, editors. 17th international school on quantum electronics: laser physics and applications. SPIE: Bellingham, USA; 2013. p. 877014.
26. Ting IP, Jolley K, Beasley CA, Pohl HA. Dielectrophoresis of chloroplasts. Biochim Biophys Acta. 1971;234:324–9.
27. Moschallski M, Hausmann M, Posch A, Paulus A, Kunz N, Duong TT, et al. MicroPrep: chip-based dielectrophoretic purification of mitochondria. Electrophoresis. 2010;31:2655–63.
28. Luo J, Abdallah BG, Wolken GG, Arriaga EA, Ros A. Insulator-based dielectrophoresis of mitochondria. Biomicrofluidics. 2014;8:21801.
29. Ermolina I, Milner J, Morgan H. Dielectrophoretic investigation of plant virus particles: Cow Pea Mosaic Virus and Tobacco Mosaic Virus. Electrophoresis. 2006;27:3939–48.
30. Green N, Morgan H, Milner JJ. Manipulation and trapping of sub-micron bioparticles using dielectrophoresis. J Biochem Biophys Methods. 1997;35:89–102.
31. Hughes MP, Morgan H, Rixon FJ, Burt JP, Pethig R. Manipulation of herpes simplex virus type 1 by dielectrophoresis. Biochim Biophys Acta. 1998;1425:119–26.
32. Müller T, Fiedler S, Schnelle T, Ludwig K, Jung H, Fuhr G. High frequency electric fields for trapping of viruses. Biotechnol Tech. 1996;10:211–26.
33. Schnelle T, Müller T, Fiedler S, Shirley SG, Ludwig K, Herrmann A, et al. Trapping of viruses in high-frequency electric field cages. Naturwissenschaften. 1996;83:172–6.
34. Gimsa J. New light-scattering and field-trapping methods access the internal electric structure of submicron particles, like influenza viruses. Ann N Y Acad Sci. 1999;873:287–98.
35. Hübner Y, Hoettges KF, McDonnell MB, Carter MJ, Hughes MP. Applications of dielectrophoretic/electrohydrodynamic "zipper" electrodes for detection of biological nanoparticles. Int J Nanomedicine. 2007;2:427–31.
36. Maruyama H, Kotani K, Masuda T, Honda A, Takahata T, Arai F. Nanomanipulation of single influenza virus using dielectrophoretic concentration and optical tweezers for single virus infection to a specific cell on a microfluidic chip. Microfluid Nanofluid. 2011;10:1109–17.
37. Masuda T, Maruyama H, Honda A, Arai F. Virus enrichment for single virus infection by using 3D insulator based dielectrophoresis. PLoS One. 2014;9:e94083.
38. Grom F, Kentsch J, Müller T, Schnelle T, Stelzle M. Accumulation and trapping of hepatitis A virus particles by electrohydrodynamic flow and dielectrophoresis. Electrophoresis. 2006;27:1386–93.
39. Nakano M, Obara R, Ding Z & Suehiro J In: 2013 seventh international conference on sensing technology (ICST). IEEE; 2013. pp. 374–8.
40. Nakano M, Ding Z, Suehiro J. Dielectrophoresis and dielectrophoretic impedance detection of adenovirus and rotavirus. Jpn J Appl Phys. 2016;55:17001.
41. Ding J, Lawrence RM, Jones PV, Hogue BG, Hayes MA. Concentration of Sindbis virus with optimized gradient insulator-based dielectrophoresis. Analyst. 2016;141:1997–2008.
42. Yamamoto T, Fujii T. Active immobilization of biomolecules on a hybrid three-dimensional nanoelectrode by dielectrophoresis for single-biomolecule study. Nanotechnology. 2007;18:495503.
43. Laux E-M, Knigge X, Bier FF, Wenger C, Hölzel R. Dielectrophoretic immobilization of proteins: quantification by atomic force microscopy. Electrophoresis. 2015;36:2094–101.
44. Laux E-M, Kaletta UC, Bier FF, Wenger C, Hölzel R. Functionality of dielectrophoretically immobilized enzyme molecules. Electrophoresis. 2014;35:459–66.
45. Knigge X, Wenger C, Bier FF, Hölzel RJ. Dielectrophoretic immobilisation of nanoparticles as isolated singles in regular arrays. Phys D: Appl Phys. 2018;51:65308.
46. Hölzel R, Pethig R. Protein dielectrophoresis: I. Status of experiments and an empirical theory. Micromachines. 2020;11:533.
47. Otto S, Kaletta U, Bier FF, Wenger C, Hölzel R. Dielectrophoretic immobilisation of antibodies on microelectrode arrays. Lab Chip. 2014;14:998–1004.
48. Stanke S, Bier FF, Hölzel R. Fluid streaming above interdigitated electrodes in dielectrophoresis experiments. Electrophoresis. 2011;32:2448–55.
49. Morgan H, Green NG. AC electrokinetics: colloids and nanoparticles. Philadelphia: Research Studies Press; 2003.
50. Green NG, Ramos A, González A, Castellanos A, Morgan H. Electrothermally induced fluid flow on microelectrodes. J. Electrostat. 2001;53:71–87.
51. Chen DF, Du H. Simulation studies on electrothermal fluid flow induced in a dielectrophoretic microelectrode system. J Micromech Microeng. 2006;16:2411–9.
52. Morgan H, Green N, Ramos A. Nano-scale AC electrokinetics and electrohydrodynamics. J Phys D: Appl Phys. 2017;50:11001.
53. Green NG, Ramos A, González A, Morgan H, Castellanos A. Fluid flow induced by nonuniform ac electric fields in electrolytes on microelectrodes. III. Observation of streamlines and numerical simulation. Phys Rev E: Stat Nonlinear Soft Matter Phys. 2002;66:26305.
54. Gonzalez A, Ramos A, Green NG, Castellanos A, Morgan H. Fluid flow induced by nonuniform ac electric fields in electrolytes on microelectrodes. II. A linear double-layer analysis. Phys Rev E: Stat Phys Plasmas Fluids Relat Interdiscip Topics. 2000;61:4019–28.
55. Ramos A, Morgan H, Green NG, Castellanos A. Ac electrokinetics: a review of forces in microelectrode structures. J Phys D: Appl Phys. 1998;31:2338–53.
56. Stokes GG. On the effect of the internal friction of fluids on the motion of pendulums. Trans Camb Philos Soc. 1851;9:8–106.
57. Friedrich A, Habl G, Sauer M, Wolfrum J, Hoheisel J, Marmé N, et al. In: Enderlein J, Gryczynski ZK, editors. Ultrasensitive

and single-molecule detection technologies II. SPIE: Bellingham, USA; 2007. p. 64440M.
58. Marmé N, Friedrich A, Denapaite D, Hakenbeck R, Knemeyer J-P. Single nucleotide polymorphism analysis using different colored dye dimer probes. Chem Phys Lett. 2006;428:440–5.
59. Landmann L. Deconvolution improves colocalization analysis of multiple fluorochromes in 3D confocal data sets more than filtering techniques. J Microsc. 2002;208:134–47.
60. Karpova TS, McNally JG, Moltz SL, Cooper JA. Assembly and function of the actin cytoskeleton of yeast: relationships between cables and patches. J Cell Biol. 1998;142:1501–17.
61. Femino AM, Fay FS, Fogarty K, Singer RH. Visualization of single RNA transcripts in situ. Science. 1998;280:585–90.
62. Sage D, Donati L, Soulez F, Fortun D, Schmit G, Seitz A, et al. DeconvolutionLab2: an open-source software for deconvolution microscopy. Methods. 2017;115:28–41.
63. Hoettges KF, McDonnell MB, Hughes MP. Use of combined dielectrophoretic/electrohydrodynamic forces for biosensor enhancement. J Phys D: Appl Phys. 2003;36:L101–4.
64. Guha S, Jamal FI, Wenger C. A review on passive and integrated near-field microwave biosensors. Biosensors. 2017;7:42.
65. Ettehad HM, Yadav RK, Guha S, Wenger C. Towards CMOS integrated microfluidics using dielectrophoretic immobilization. Biosensors. 2019;9:77.

How to cite this article: Stanke S, Wenger C, Bier FF, Hölzel R. AC electrokinetic immobilization of influenza virus. Electrophoresis. 2022;1–13. https://doi.org/10.1002/elps.202100324